COMPUTED ELECTRON MICROGRAPHS FOR TILTED FOILS CONTAINING DISLOCATIONS AND STACKING FAULTS

By P. HUMBLE*

[*Manuscript received December* 18, 1967]

Summary

The method of computation of electron microscope images developed by Head (1967) produces micrographs of single dislocations in about 1 min of numerical integration. In Head's original programme, the electron beam direction and the normal to the foil surface are coincident. Since this condition is not often realized in practical electron microscopy, the programme has been extended to compute the images of dislocations in tilted foils. It has been further modified to compute the images from a configuration containing up to two dislocations and up to three stacking faults. These programmes are thus applicable to a wide range of defect configurations in tilted thin foils. The derivation of these programmes is described and several examples of their use in experimental situations are given. These include the "skewing" of dislocation images due to the noncoincidence of the beam direction and the foil normal, and images due to interactions between dislocations and stacking faults.

I. INTRODUCTION

Until recently, computations of the intensity of electron microscope images of dislocations and other defects in thin foils have been limited to graphs (or profiles) of the way in which the intensity of the image varies along a line crossing the defect. These profiles are not continuous curves but consist of discrete points, each of which has been computed by a separate numerical integration. Thus, the computation of several profiles takes a considerable amount of computer time. In addition, it is often difficult to interpret the profiles in terms of an actual experimental micrograph of the defect, since the experimental counterpart of a profile, namely a microphotometer trace across the defect, is seldom used. Indeed, the profiles are usually translated into the form of a picture mentally by the observer. Hence, the computation of complete theoretical pictures of a defect which can be compared directly with experimental micrographs would be extremely helpful in reducing the subjectiveness of the comparison.

In a recent paper, Head (1967) has described a way of producing computer-simulated images of dislocations in which all the information required can be obtained in about 1 min of numerical integration of the Howie–Whelan (1961) differential equations for two-beam electron diffraction. This information is presented, not in the form of profiles, but in the form of a half-tone picture using the computer line

* Division of Tribophysics, CSIRO, University of Melbourne, Parkville, Vic. 3052.

printer. Head has shown that when the important information is contained in the topology of the image, as is generally the case, such theoretical "micrographs" are extremely valuable.

In the programme developed by Head, the normal to the foil surface and the electron beam direction are coincident. However, tilting devices in electron microscopes may commonly tilt the specimen up to $\pm 30°$ and such noncoincidence of the foil normal and electron beam direction must be taken into account in direct comparisons between experimental and computed images. Section II(a) deals with the derivation of a computer programme of the type described by Head which takes into account any given foil normal. Section II(b) outlines the extension of this programme to the case of two parallel dislocations connecting three stacking faults. Simpler configurations than are allowed for in Section II(b) can be obtained by putting the appropriate Burgers vectors and/or the shears on the planes to zero.

Section III describes some of the uses of these programmes and compares the computed and experimental images of several defects.

II. Computations

Following Head, we consider only straight dislocations sloping through a foil of constant thickness t. Since we consider only configurations consisting of single dislocations or dislocations that are parallel, and since no surface relaxations are allowed, the elastic displacement field of the dislocations is constant along any line parallel to them. This is true even when the displacement fields are computed in full elastic anisotropy, as is the case here. With the foregoing restrictions, it is possible to define a "generalized cross section" (Head 1967) that, for a given dislocation, has a fixed displacement field. On this cross section a pair of lines of constant separation, but variable position, can represent the foil surfaces and delineate the parts of the displacement field through which the electron beam passes for the various profiles.

The equations of Howie and Whelan (1961, equations (5)), based on a two-beam column approximation (including absorption), describe the dynamical interaction of the electron beam with the displacement field. These equations are a pair of first-order linear differential equations in T' and S', the transmitted and scattered amplitudes respectively, and thus have only two independent solutions. If these are known, all other solutions may be obtained by taking linear combinations of them.

The speed of Head's method of producing theoretical micrographs comes from combination of the facts that a generalized cross section, in which the displacement fields are fixed, *can* be established and that only *two* numerical integrations per column of this cross section, followed by linear combinations of solutions, provides the information for corresponding points on many profiles. Previous methods have used a separate integration for each point on each profile. The problem, therefore, in applying this method to other configurations is to establish the generalized cross section for the configuration being considered and to define the way in which the integrations are to be done so that the appropriate linear combinations may be chosen.

(*a*) *Generalized Cross Section for Tilted Foil*

Figure 1(*a*) shows a dislocation sloping through an untilted foil in the manner considered by Head. The dislocation enters the bottom surface of the foil on the line HG and leaves the top surface on the line LM. The vertical lines in Figure 1(*a*) are parallel to the beam direction. The generalized cross section for this configuration is obtained by projection in a direction parallel to the dislocation onto the plane LMNO. This generalized cross section is shown in Figure 1(*b*). The dislocation is coming out of the paper but is not normal to it. The dashed letters in Figure 1(*b*) correspond to the undashed letters in Figure 1(*a*). Note that the line HG projects into H′G′, which is coincident with L′M′, the projection of LM. Lines E′F′ and H′G′ represent the top and bottom surfaces of the foil respectively for the profile in which the dislocation is just entering the bottom of the foil; L′M′ and O′N′ represent the top and bottom surface of the foil for the profile in which the dislocation is just leaving the top of the foil. Intermediate profiles on, for example, the shaded plane shown in Figure 1(*a*), are obtained by taking the portion of the displacement field between the two dashed lines on the generalized cross section in Figure 1(*b*).

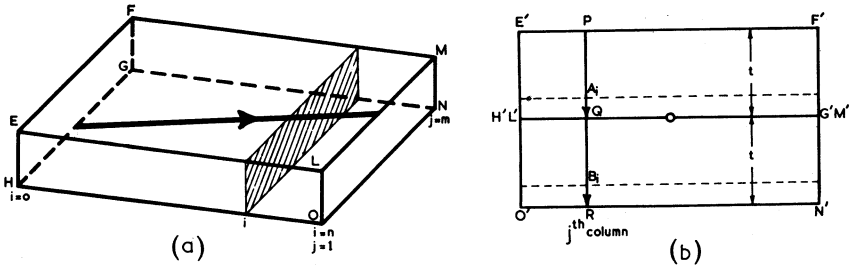

Fig. 1.—Geometry (*a*) and generalized cross section (*b*) for a single dislocation in an untilted foil.

The amplitudes T' and S' are integrated down columns in the cross section parallel to the beam direction. An equal number of columns on either side of the dislocation is considered, care being taken not to integrate down a column that is within one-quarter of the normal column spacing of the dislocation core. If columns closer to the dislocation core are considered, the programme takes an excessive amount of time to integrate through the rapidly changing strain field.

Consider the jth column from the dislocation as shown in Figure 1(*b*). The integration down this column is done in two main parts, the first part (A) from P to Q and the second part (B) from Q to R. Each part is divided into n steps of equal size. Two beams, with independent initial amplitudes at the top of the cross section are integrated down the column simultaneously, and the amplitudes at the end of each step stored in the computer memory. The intensity of the image for the surfaces of the foil in the positions shown by the dashed lines in Figure 1(*b*) is obtained by combining the two solutions for the position A_i with the two for the position B_i linearly and in such a manner as to give the correct boundary conditions for the top surface of the foil; that is, $T' = 1$ and $S' = 0$ at A_i.

By allowing i to run from 0 to n, we obtain $n+1$ values of the intensity for the jth column in successive profiles running from the plane EFGH to the plane LMNO in Figure 1(a). Thus we have $n+1$ intensity values to establish the points on one row of the theoretical micrograph parallel to the dislocation line. By repeating the procedure for $j = 1$ to m, we obtain the m rows of the picture. In the present case, $n = 128$ and $m = 60$. The spacing of the columns and the rows is related to the intercharacter spacing on the line printer so that the magnification across the picture is the same in all directions and all angles are true.

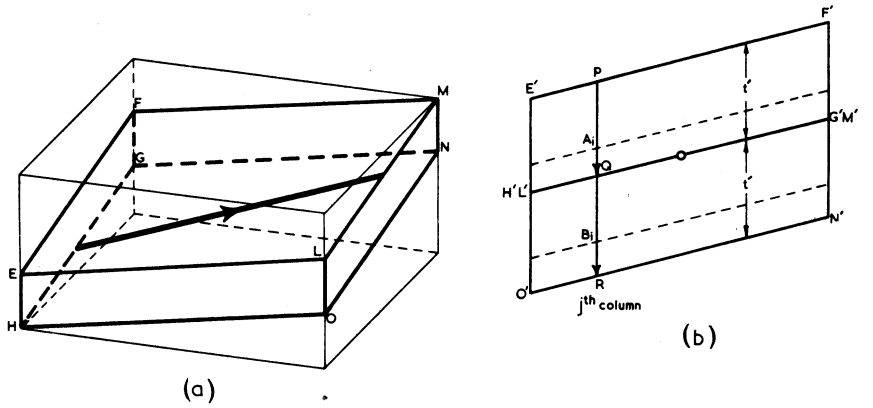

Fig. 2.—Geometry (a) and generalized cross section (b) for a single dislocation in a tilted foil.

The case of a tilted foil is shown in Figure 2. As in the previous case, Figure 2(a) considers just that part of the foil that bounds the ends of the dislocation, and the generalized cross section shown in Figure 2(b) is obtained by projection of Figure 2(a) along the dislocation direction onto the plane LMNO. Thus, the projections of HG and LM are coincident.

As in the case of untilted foils, the integration is carried out in two parts PQ and QR, and the rows of the picture obtained in a similar way. However, there are two modifications that have to be made. Firstly, PQ and QR are now each equal to t', rather than t, where t' is the thickness of the foil in the direction of the beam. Secondly, the integration in each column of the generalized cross section is started on the line E'F', but this line is now at an angle to the beam that is determined by the component of tilt of the foil in the generalized cross section plane. The other component of tilt of the foil is automatically taken into account by this method of forming the picture.

(b) *Generalized Cross Section for Tilted Foil involving Dislocations and Stacking Faults*

It was mentioned at the beginning of this section that, provided cases involving more than one dislocation are restricted to configurations of parallel dislocations, a generalized cross section can still be defined. The corresponding restriction on the geometry of stacking faults is that the faulted planes must contain the dislocation direction. Thus the generalized cross section for one possible configuration involving

two dislocations and three stacking faults is shown in Figure 3(*b*). The faulted planes are shown as dotted lines, dislocation *X* being at the intersection of planes *a* and *b*, and dislocation *Y* at the intersection of planes *b* and *c*. The corresponding view of the tilted foil is shown in Figure 3(*a*), but here, for the sake of clarity, only one faulted plane (*b*) has been shaded.

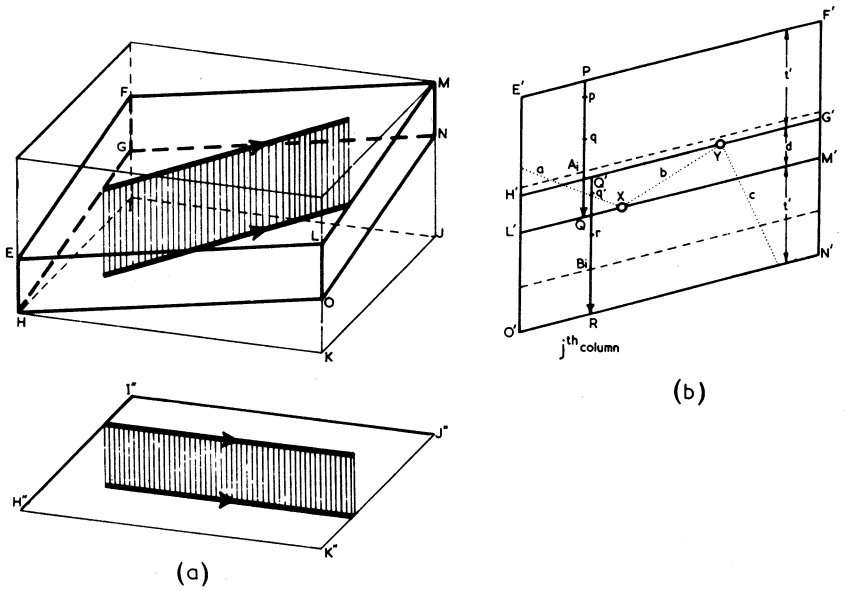

Fig. 3.—Geometry (*a*) and generalized cross section (*b*) for two dislocations and three stacking faults in a tilted foil. In (*a*) only the central fault has been shown, and the projection H"I"J"K" illustrates the arrangement of the dislocations and the central stacking fault in the computed micrograph.

The portion of the foil shown in Figure 3(*a*) is bounded in a similar way to that shown in Figures 1(*a*) and 2(*a*), being that portion which just contains the dislocations. The layout of the computed picture is obtained by projection onto the plane HIJK, and this is shown in the lower part of Figure 3(*a*). With this geometry, the generalized cross section is obtained, as before, by projection in the dislocation direction onto the plane LMNO. Note, however, that now the projections of HG and LM are no longer coincident, but are separated by an amount d measured in the direction of the electron beam. The corresponding two ranges of integration for parts A and B are now PQ and Q'R, where $PQ = Q'R = t' + d$. For clarity, PQ and Q'R are shown as separate arrows in Figure 3(*b*); in fact, they both refer to integrations carried out down the same (jth) column.

As before, PQ and Q'R are each divided into n equal steps and the amplitudes integrated down the column of the cross section. However, before integrating through each step note is taken whether a stacking fault occurs in this step, or perhaps the position Q' at which the B part of the integration starts. If a stacking fault does occur in the particular step, the integration is stopped at the fault, the scattered waves are changed in phase (determined by the shear on the plane), and the

integration then continued to the end of the step. If the point Q′ occurs in a step, the amplitudes of the transmitted and scattered waves at this point are stored in the computer memory and, after the completion of the A part of the integration, are put into the integration programme as the starting conditions for the B part of the integration.

As mentioned earlier, many different geometrical arrangements containing up to two dislocations and up to three stacking faults are possible with the configuration depicted in Figure 3, since either of the Burgers vectors and/or the shears on the faulted planes may be zero. Also, the programme is not limited to non-overlapping stacking faults, as shown in Figure 3(*b*), but can compute the contrast from two or three overlapping faults. Of course this programme, in common with the ones described in Section II(*a*), computes the contrast from the dislocations using the full anisotropic elastic strain fields of these defects.

An important variation of the basic programme is obtained by restricting the ranges of integration, to pq and q′r, for example, in Figure 3(*b*). In this way, it is possible to frame the computed picture so that any part of the dislocation length in the foil is shown in the picture. This has the effect of increasing the magnification and the resolution of the computed micrograph. This is extremely useful in making detailed comparisons between computed and experimental images.

In addition to the micrographs of the many stacking-fault and dislocation configurations that it is possible to compute with these programmes, it is also possible, in some cases, to compute the images of more complex configurations by making the total image from a composite of two or more computed micrographs. This is an allowed procedure only when there are no dislocations present, or when the dislocation strain fields are negligible at the place where the micrographs are joined.

III. Discussion and Examples of Use of the Programmes

Figure 4(*a*) shows the computed image of a pure screw dislocation in β-brass. The Burgers vector **b** is $[\bar{1}\,11]$, the reflecting vector **g** is $[\bar{1}\bar{1}0]$, and the beam direction **B** and the foil normal **F** are both $[001]$. It can be seen that the image is symmetrical either side of the dislocation line. It consists of oppositely positioned black dots along the line of the dislocation, with a region shaped like an arrow head where the dislocation leaves the top surface of the foil and a marked white region just before the dislocation leaves the bottom surface.

Figures 4(*b*) and 4(*c*) are images of the same dislocation under the same diffracting conditions, except that the foil normal has been moved away from $[001]$ in a direction that is normal to the dislocation line in the image. For Figure 4(*b*) **F** = $[115]$ and for Figure 4(*c*) **F** = $[113]$. It is apparent that the effect of varying the foil normal in this way is to "skew" the image. The dots in the image no longer correspond exactly across the dislocation line, but have been displaced in directions parallel to this line in opposite senses on either side of the line. This effect was predicted by Head, Loretto, and Humble (1967), but is extremely difficult to detect with the profile method of image computation.

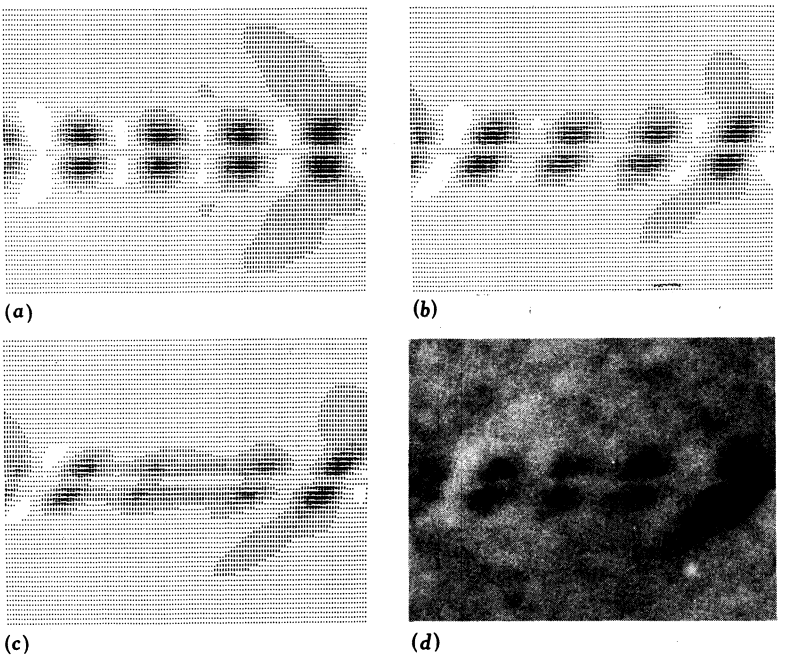

(a) (b) (c) (d)

Fig. 4.—Micrographs of a screw dislocation of Burgers vector $[\bar{1}11]$ in β-brass using the $[\bar{1}\bar{1}0]$ reflecting vector in the [001] beam. The computed micrographs have foil normals of [001] in (*a*), [115] in (*b*), and [113] in (*c*). The foil normal for the experimental micrograph in (*d*) is [115].

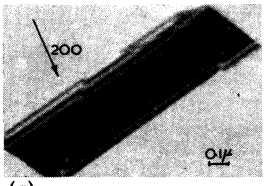

(a)

Fig. 5.—Theoretical micrographs (*b*) and (*c*) computed using two different contrast scales. The geometry and diffracting conditions are the same as for the central portion of the complex Frank loop shown in the experimental micrograph in (*a*).

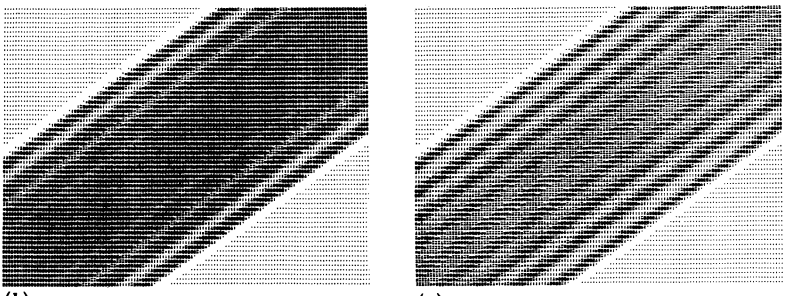

(b) (c)

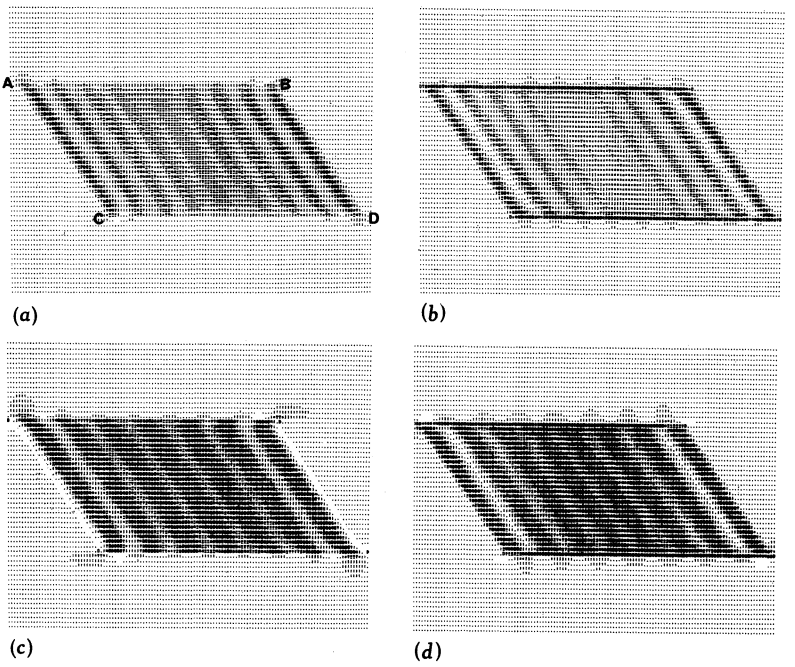

Fig. 6.—Computed micrographs illustrating the effect on the dislocations AB and CD bounding a faulted Frank loop of reversing the reflecting vector from [0$\bar{2}$0] in (*a*) and (*c*) to [020] in (*b*) and (*d*). For (*a*) and (*b*) w is 0·9 and for (*c*) and (*d*) w is 0·3. Note the variations in the intensity and spacing of the fault fringes and the change in contrast of the fringes close to the surfaces of the foil AC and BD.

Fig. 7(*opposite*).—A Frank dislocation loop ABHG and a glide dislocation CDEF taken on four different reflecting vectors. Note that in (*d*) the portions CD and EF of the glide dislocation are virtually out of contrast whereas the segment DE, which passes close to the fault, shows a strong image.

Fig. 8(*opposite*).—Computed micrographs corresponding to the areas of the experimental micrographs outlined by dashed lines in Figure 7.

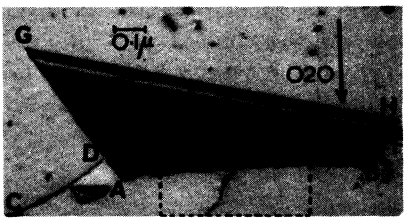

(a)

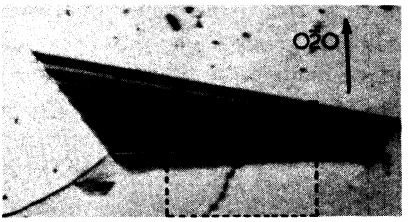

(b)

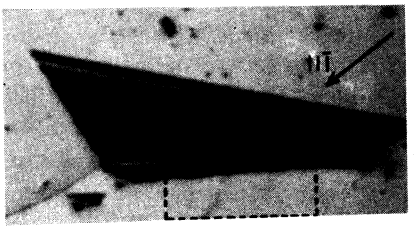

(c)

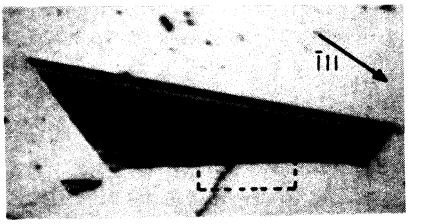

(d)

Fig. 7

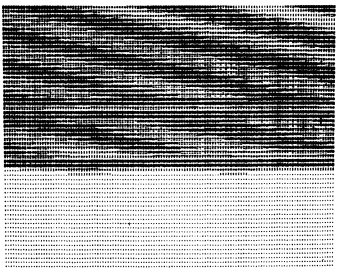

(a)

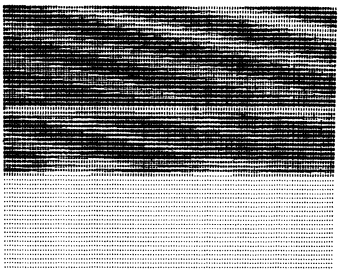

(b)

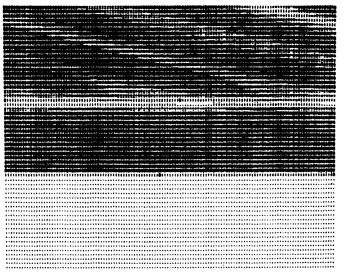

(c)

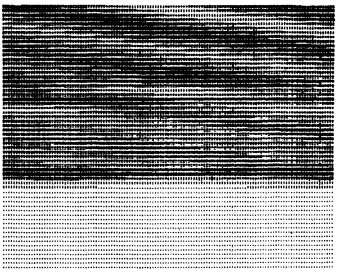

(d)

Fig. 8

Figure 4(*d*) shows the experimental image of such a screw dislocation of $\mathbf{b} = [\bar{1}11]$ in β-brass. The diffraction conditions are the same as those used for the computed micrographs in Figures 4(*a*)–4(*c*). The foil normal for this specimen is very close to [115]. Hence, this experimental micrograph may be compared directly with the computed micrograph in Figure 4(*b*), and in fact the angles through which the images are skewed are almost exactly the same.

The choice of the scale of grey to be used for images of different types of defects has been discussed by Head (1967), who suggested, for example, that the visibility of stacking-fault fringes might require a different scale from that used for dislocation images. Figure 5(*a*) shows a complicated faulted loop in a quenched copper–aluminium (9%) alloy and Figure 5(*b*) shows the computed image corresponding to the central portion of this defect. The fringes in the middle of the computed image become indistinct in Figure 5(*b*), whereas they are clearly visible in the experimental micrograph. In fact, it is possible to vary both the contrast (the apportioning of the grey scale symbols to the intensity values) and the exposure (the symbol in the grey scale which represents background intensity) of the computed pictures. Figure 5(*c*) shows a computed micrograph of the central portion of the loop in Figure 5(*a*) with a grey scale of less contrast, and now the fringes are plainly visible in the middle of the image. The contrast of the grey scale used in Figure 5(*b*) is the one generally used for images involving only dislocations and is such that the symbol representing background intensity (a full stop) changes to its neighbouring symbols (a blank and a colon) at 15% above and 7% below background intensity. The contrast used for the image shown in Figure 5(*c*) has visibility limits 26% above and 14% below background intensity. Although the visibility limits for the first scale are close to the estimated experimental visibility limits for electron images, those of the second scale are not. However, it must be remembered that since the exposure, development, and printing of experimental micrographs are often chosen to enhance the detail in the particular defect under observation, there is often a large variation in the photographic parameters from one experimental image to another. It is considered, therefore, that the grey scale for computed micrographs may be chosen on a similar basis, variations in the grey scale being selected to enhance the visibility of a particular defect.

The programmes may, of course, be used to form pictures for many of the contrast effects described in the literature, and previously only illustrated by intensity profiles. For example, Silcock and Tunstall (1964) have shown that, for 020 reflecting vectors, a Frank dislocation will be out of contrast when $\mathbf{g}.\mathbf{b} = -\frac{2}{3}$ but in contrast when $\mathbf{g}.\mathbf{b} = +\frac{2}{3}$, provided that the deviation from the Bragg condition w is large ($w \sim 0{\cdot}9$).

Figures 6(*a*) and 6(*b*) show the computed images for a faulted Frank loop, in which only the opposite parallel edges are included. The direction of these dislocations $\mathbf{u}$ is $[0\bar{1}1]$. Comparing this configuration with that shown in Figure 3(*a*), the shears on planes *a* and *c* are zero, plane *b* is (111), and the dislocations *X* and *Y* have Burgers vectors $\frac{1}{3}[111]$ and $\frac{1}{3}[\bar{1}\bar{1}\bar{1}]$ respectively. The Burgers vectors refer to the same loop and yet have opposite signs because the programme is arranged so that the dislocation directions are constrained to have the same positive sense. The electron beam direction

and the foil normal are both [101] and the reflecting vectors are $[0\bar{2}0]$ ($\mathbf{g}.\mathbf{b} = -\frac{2}{3}$) in Figure 6(*a*) and [020] ($\mathbf{g}.\mathbf{b} = +\frac{2}{3}$) in Figure 6(*b*). The value of w is 0·9. The dislocations run from A to B and from C to D, and the fringe direction is parallel to the intersection of the fault plane with the surface, AC or BD. Figures 6(*c*) and 6(*d*) show the same portion of the Frank loop under the same reflecting conditions, except that the value of w is now 0.3. It is immediately apparent that the difference in contrast of the dislocations observed between Figures 6(*c*) and 6(*d*) (the small w case) is not nearly so marked as in Figures 6(*a*) and 6(*b*) (the large w case). Closer inspection shows, however, that this effect is so marked in Figures 6(*a*) and 6(*b*) not because the dislocation images themselves are markedly blacker, but mainly because the higher value of w has decreased the contrast in the fringes in these pictures, allowing the dislocation images to be clearly seen. The case computed here corresponds to the case for which $\mathbf{g}.\mathbf{b}\times\mathbf{u} \neq 0$ in Silcock and Tunstall (1964).

It should be noted that these pictures also illustrate that reversing the reflecting vector produces a change in the shade of the outermost fringe (Hashimoto, Howie, and Whelan 1962). For Figures 6(*c*) and 6(*d*), where w is small, this effect is most marked; the outermost fringe is white in Figure 6(*c*), $\mathbf{g} = [0\bar{2}0]$, and black in Figure 6(*d*), $\mathbf{g} = [020]$. For $w = 0{\cdot}9$ the outermost fringe in the image for $\mathbf{g} = [0\bar{2}0]$ (Fig. 6(*a*)) is not visibly lighter than background intensity, although measurement of the relative widths of the images in Figures 6(*a*) and 6(*b*) shows that a similar reversal occurs here also. The larger number of fringes for the larger value of w is also a characteristic effect in the imaging of stacking faults.

Figures 7(*a*)–7(*d*) are electron micrographs of a Frank dislocation loop with a glide dislocation running very close to it. The different reflecting vectors are indicated on the micrographs. For Figures 7(*a*), 7(*b*), and 7(*d*) the beam direction is [101] and for Figure 7(*c*) [213]. The foil normal is close to [407]. One edge of the loop lies along AB, which is the $[\bar{1}01]$ direction, and the glide dislocation runs along CDEF, AB and DE being almost parallel. The loop intersects one surface of the foil along GH. Figures 8(*a*)–8(*d*) show theoretical micrographs computed for the corresponding diffraction conditions and for the same geometry as in Figure 7, except that AB and DE have been made exactly parallel. The dislocation DE is 12 Å above the plane of the loop in the computed micrographs. The Burgers vector of the Frank dislocation is $\frac{1}{3}[111]$ and that of the glide dislocation $\frac{1}{2}[\bar{1}\bar{1}0]$. The range of integration used to produce these pictures has been restricted (c.f. Section II(*b*)) thus giving theoretical micrographs that cover a thickness of just one or two extinction distances within the foil, which is eight extinction distances thick for Figures 8(*a*) and 8(*b*) and nine extinction distances thick for Figures 8(*c*) and 8(*d*). Thus the computed micrographs correspond to areas about equal to those shown by the dashed lines in Figures 7(*a*)–7(*d*). This restriction is necessary to obtain the resolution in the fine detail of the image of the dislocation passing over the fault. For example, the image of this dislocation in Figure 7(*b*) consists of a black line and a white line each about 100 Å wide. These lines are reproduced in Figure 8(*b*), where 100 Å corresponds to the height of two rows of print. Using this technique of restricted ranges of integration to vary the magnification of the computed micrograph, it has been possible to match detail in experimental micrographs that is of the order of 20 Å wide.

In Figures 7(*d*) and 8(*d*) the value of $\mathbf{g}.\mathbf{b}$ is zero for the glide dislocation. Although this is not a pure screw dislocation and, therefore, cannot be completely out of contrast, the residual intensity in the portions of the dislocation CD and EF that are outside the loop is very small. However, it is interesting that, where this dislocation passes close to the loop and the stacking fault fringe contrast is present, there is a very definite image consisting of two thin black lines separated by a thin white line.

The foregoing examples illustrate some of the uses of computer programmes that produce theoretical electron micrographs. The programmes are capable of handling all the conditions of two-beam electron diffraction, the full geometry and anisotropic strain fields of many dislocation and stacking-fault configurations, and variations in photographic parameters. For images in which the information is contained in the topology of the image rather than its intensity, these programmes enable experimental images to be accurately matched. The examples of the use of the programme given here have been confined solely to the accurate reproduction of simple, and in some cases, well known, dislocation and fault configurations. However, the main usefulness of the programmes lies in the matching of computed and experimental images of less well understood defect configurations with the consequent determination of their geometry, their Burgers vectors, and their fault shears.

IV. Acknowledgments

The author wishes to thank Dr. M. H. Loretto for allowing him to use the electron micrograph shown in Figure 4(*c*), and Dr. L. M. Clarebrough for the use of the electron micrographs in Figures 5(*a*) and 7. He also wishes to acknowledge many helpful discussions with Dr. A. K. Head, and to thank Dr. L. M. Clarebrough and Dr. A. J. Morton for their comments on the manuscript.

V. References

Hashimoto, H., Howie, A., and Whelan, M. J. (1962).—*Proc. R. Soc.* A **269**, 80.
Head, A. K. (1967).—*Aust. J. Phys.* **20**, 557.
Head, A. K., Loretto, M. H., and Humble, P. (1967).—*Phys. Status Solidi* **20**, 505.
Howie, A., and Whelan, M. J. (1961).—*Proc. R. Soc.* A **263**, 217.
Silcock, J. M., and Tunstall, W. J. (1964).—*Phil. Mag.* **10**, 361.